IEEE Access
Multidisciplinary ⋮ Rapid Review ⋮ Open Access Journal

Received January 16, 2022, accepted January 18, 2022, date of publication January 27, 2022, date of current version February 4, 2022.

Digital Object Identifier 10.1109/ACCESS.2022.3146826

Design and Characteristic Analysis of a New Dual-Stator Bearingless Switched Reluctance Motor

NING HAN[1], CHUANYU SUN[2], JIAQING LI[1], HANG YANG[3], AND SHANGKE HAN[3]

[1]College of Mechanical and Electronic Engineering, Shandong University of Science and Technology, Qingdao 266590, China
[2]School of Automation and Electrical Engineering, Linyi University, Linyi 276005, China
[3]College of Ocean Science and Engineering, Shandong University of Science and Technology, Qingdao 266590, China

Corresponding author: Chuanyu Sun (13708983820@163.com)

This work was supported in part by the Natural and Science Foundation of China under Project 51774193, in part by the Natural and Science Foundation of Shandong Province under Project ZR2019MEE068, in part by the Application Scientific Research of Qingdao City under Project 15-9-1-66-jch, and in part by the Postdoctoral Research Foundation of Qingdao City under Project 01020120521.

ABSTRACT This paper proposes a 18/15/6 pole dual-stator bearingless switched reluctance motor (DSBSRM) with better overall performance. The proposed motor separates the torque control system and the suspension control system with a magnetic isolation ring. The torque drive system adopts the method of optimizing the distribution and quantity of the stator and rotor tooth poles, which reduces the hysteresis force that exists during the commutation of the electromagnetic poles and improves the torque output capacity and the electromagnetic conversion efficiency. The suspension control system adopts hybrid excitation differential control method. This method increases the electromagnetic induction intensity of the suspension system at a small current and thus improves the levitation force output capability and control accuracy. The mathematical model of the 18/15/6 pole DSBSRM was established. The torque mathematical model adopts the Maxwell stress integral method after path optimization, and the levitation mathematical model is established with full consideration of the rotor offset problem to ensure the accuracy of the mathematical model. Ansoft Maxwell 2D software was then used to simulate the 18/15/6 pole DSBSRM in 2D. While verifying the correctness of the mathematical model, the characteristics of the motor were analyzed and the influence of key parameters such as control current and air gap thickness on the performance of the motor was analyzed. In order to further highlight the excellent performance of 18/15/6-pole DSBSRM. Compare 18/15/6 pole DSBSRM with new 16-phase BSRM and 12/8/4 pole DSBSRM. Structural decoupling method is used in all 3 motors. The results show that the proposed 18/15/6-pole DSBSRM has better performance in terms of torque and suspension output capacity and decoupling performance.

INDEX TERMS BSRM, hybrid excitation, magnetic field decoupling, mathematical model, differential control, performance analysis.

I. INTRODUCTION

With the development of magnetic bearing technology, applying magnetic levitation technology to switched reluctance motors(SRM), bearingless switched reluctance motors(BSRM) are produced [1]–[4]. The bearingless switched reluctance motor is based on the ''principle of minimum reluctance'' [5]–[7]. It effectively solves the problems of severe heat generation and low service life caused by the relatively serious friction of the rotor in the traditional SRM during high-speed rotation. Improve the critical speed and service life of the motor [7]–[9]. At the same time, it inherits the high reliability and excellent speed regulation performance of the SRM, which has been a research hotspot in the motor field in the past two decades. It can be promoted in many practical industrial fields such as flywheel energy storage systems, electric vehicles, aerospace, etc., [10], [11].

The concept of BSRM was first proposed by Japanese scholars in 1989, and in the 1990s a team of Japanese scholars proposed a 12/8 pole DSBSRM and carried out research on the torque and control of BSRM, followed by many scholars in various countries and other countries to carry out research

The associate editor coordinating the review of this manuscript and approving it for publication was Mauro Gaggero.

and optimization of BSRM [1], [12]. Conventional BSRMs produce both electromagnetic torque and levitation forces when operating with varying inductance between the stator and rotor. So, either adjusting the torque or the levitation force will have an effect on the other output. In addition, when the windings are energized, the magnetic field lines that generate torque and levitation force are interlinked, which leads to the coupling of torque control and levitation control [13]. The two main methods of decoupling the BSRM torque and levitation forces are algorithmic decoupling and structural decoupling. Algorithmic decoupling uses control algorithms to adjust and distribute the torque and suspension current components in real time but is more difficult and susceptible to external interference. Structural decoupling eliminates and reduces the coupling of torque and levitation force by improving the motor structure, which reduces the control difficulty and ensures the reliability of the BSRM. With the continuous research in recent years the commonly used structural decoupling have divided into the following four categories: mixed stator tooth types such as the 12/14 pole mixed stator tooth BSRM proposed in the literature [14]; wide rotor tooth structures such as the new 16 phase BSRM proposed in the literature [13]; double stator structures such as the 12/8/4 pole DSBSRM proposed in the literature [15]; composite rotor structures such as the 12/8 pole single winding composite rotor BSRM proposed in the literature [16].

This article focuses on the application of bearingless switched reluctance motor in artificial heart. Based on the summary of existing research, proposes a bearingless switched reluctance motor with superior comprehensive performance and good decoupling performance to meet the requirements of replacing the heart. Compared with the conventional BSRM, this motor has two stators, the torque stator and the suspension stator, has the optimized teeth number of stator and rotor for better performance, has a hybrid excitation suspension output system. A mathematical model of the motor was derived using Maxwell'2D stress method, and then the motor performance was analyzed and verified by finite element simulation software. Finally, the performance of 18/15/6 pole DSBSRM is compared with 12/8/6 pole DSBSRM and new 16 phase BSRM, which are also structurally decoupled, to verify the outstanding performance of 18/15/6 pole DSBSRM.

II. MOTOR STRUCTURE

This paper proposes a new type of BSRM, as shown in Fig.1(a)(b). The stator section consists of an 18-pole outer stator, a 6-pole inner stator, a stator torque winding, a permanent magnet and a levitation control winding, where the inner stator consists of a 3-phase winding control pole and a 3-phase permanent magnet control pole; the rotor section consists of a 15-pole torque rotor and a levitation rotor ring connected by a magnetic isolation material to form a whole.

For the winding of the motor, as shown in Fig.2, the torque winding on the outer stator is divided according to the structure of the 18 outer stator teeth into 3 phases separated by 40°.

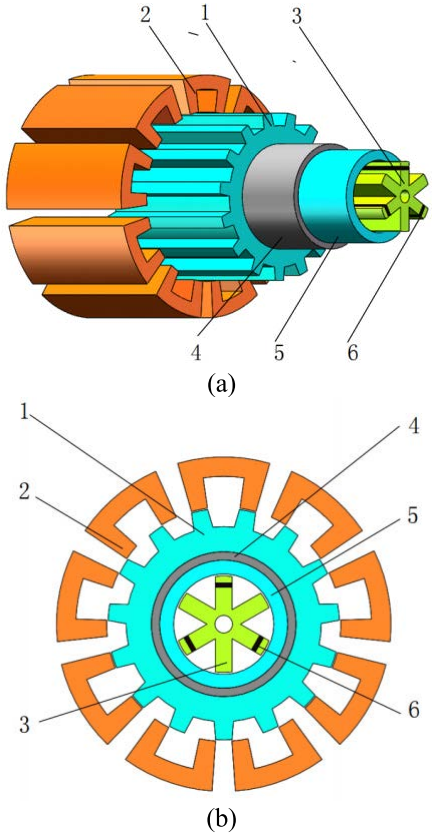

1 - Torque rotor; 2 - Outer stator; 3 - Inner stator; 4 - Isolation ring; 5 - Suspended rotor ring; 6 - Permanent magnet

FIGURE 1. 18/15/6 Pole DSBSRM motor structure. (a)18/15/6 pole DSBSRM exploded view. (b) 18/15/6 pole DSBSRM end view.

Each phase containing 3 pairs of stator windings separated by 120°, each pair of adjacent stator windings separated by 24°. As shown in Fig.2, A1 and A2 are a pair of adjacent windings. The winding method is single winding, with opposite windings on each pair of stator teeth, all windings have the same number of turns, and each phase can be controlled independently. Taking phase A as an example, there are two pairs of coil windings of which A_1 and A_2 are wound on two adjacent stator teeth as a pair of poles; A_3 and A_4 are wound on two other adjacent stator teeth as a pair, and A_5 and A_6 are wound on the third pair of stator teeth as a pair of poles, which are then connected in series to form phase A winding. The presence of six torque teeth in each phase of the torque winding further improves the efficiency of the torque output. At the same time, the levitation forces produced by 3 pairs of poles in the same phase counteract each other, which reduces the influence of torque system on suspension system. The same winding principle as the A-phase winding forms the B-phase and C-phase windings together with the A-phase winding to form a 3-phase torque winding.

The suspension winding adopts the method of hybrid excitation on the inner stator. The 3 teeth of the inner stator are the permanent magnet poles and the other 3 stator teeth are the control poles, each pole is equally distributed on the inner

stator. As shown in Fig.2, 3 permanent magnet poles N_1, N_2 and N_3 are located at 0°, 120° and 240° positions. The three control poles are located in the directions of 60°, 180° and 270°. The 3 permanent magnet poles have the same structure, the same size, and the same material. The 3 permanent magnets radial magnetization direction is also from the inner stator center to outward. The 3 control windings M_1, M_2 and M_3 with the same winding mode on the control poles, which act in conjunction with the permanent magnet poles to control the rotor suspension.

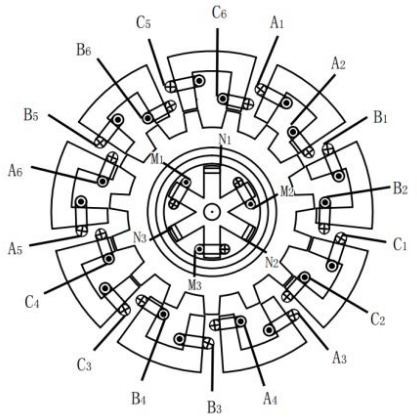

FIGURE 2. 18/15/6 Pole DSBSRM winding method.

III. WORKING PRINCIPLE AND MATHEMATICAL MODEL DERIVATION

A. TORQUE

Under ideal conditions, BSRM follow the "principle of minimum reluctance". Fig.3 shows the principle of torque generation in motor operation. When phase A is energized, the magnetic field lines generated by the torque winding will enter the adjacent torque teeth, forming a closed loop of magnetic field lines of "stator tooth - air gap - torque tooth - air gap - stator tooth" represented by the solid red line in the figure [17], [18]. Therefore, a counterclockwise torque is generated, and counterclockwise is the positive direction. When the rotor passes through a stepping angle and the rotor tooth is completely aligned with the stator tooth of phase A, the phase A winding is energized and the phase B winding is de-energized. In this way, the 3 phases are connected in sequence to form a "A→B→C→A" cycle, so that the motor works normally.

Before modelling, the following assumptions are made:

The magnetic circuit saturation is ignored, and the eccentric displacement of the rotor is not considered;

The magnetic flux density distribution in stator, rotor teeth and air gap is uniform;

When the stator and rotor teeth are perfectly aligned, the edge magnetic fluxes on both sides have the characteristics of center symmetry.

Maxwell stress tensor is an extension of Maxwell electromagnetic theory, which can show the interaction between

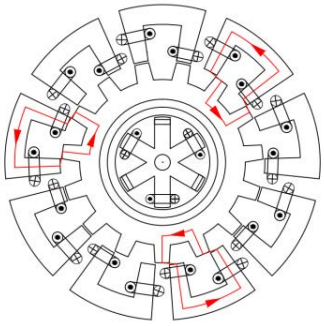

FIGURE 3. Equivalent magnetic circuit diagram of the torque principled.

electric field force, magnetic field force and mechanical momentum. The content is: the tension component of the magnetic field is the same as the effect of a qualitative dynamics. The normal force and tangential force of the magnetic stress acting on the curved surface s can be expressed as [19], [20]:

$$F_n = \frac{1}{2\mu_0} \iint_S \left(B_n^2 - B_t^2\right) dA \tag{1}$$

$$F_t = \frac{1}{\mu_0} \iint_S B_n B_t dA \tag{2}$$

where: μ_0 is the vacuum permeability, B_n and B_t are the normal and tangential components of the air gap flux density.

The traditional Maxwell stress method is used to integrate paths consisting only of paths perpendicular and parallel to the magnetic lines of force in Fig.4(a). Although it reduces the computational effort, it also reduces the model accuracy. In order to overcome the limitations of the traditional Maxwell stress method of path selection. A new area integration path is selected as segments 1 to 8 in Fig.4(b). The radian of stator and rotor teeth is 8°. Set counterclockwise as the positive direction, then in the figure $\theta \leq 8°$.

According to Maxwell's stress method combined with (1) and (2). As shown in Fig.4, the electromagnetic torque T_1 applied to the rotor at the air gap at position $\theta \in [0°, 8°]$ is obtained as follows:

$$T_1 = \frac{hr_0}{2\mu_0} \begin{pmatrix} \int_3^4 B_m^2 dl + \int_5^6 B_f^2 sin\tau dl \\ - \int_6^7 B_m^2 dl + \int_7^8 B_f^2 sin\tau dl \end{pmatrix} \tag{3}$$

where: dl is the integral path length unit. τ is the angle between the normal vector of the integral path and the centre line of the rotor tooth poles. B_m is the main air gap flux and B_{f1} is the air gap edge flux.

In the process of one-phase being powered, six teeth are in the same work state. According to the motor structure and (3), the torque mathematical model of the 18/15/6 pole DSBSRM based on Maxwell stress method is as follows:

$$T = 6T_1, \quad \theta \in \left[0, \frac{\pi}{45}\right] \tag{4}$$

The air-gap magnetic resistance of the windings is indicated by R_{A1} and R_{A2}, i indicates the energising current of

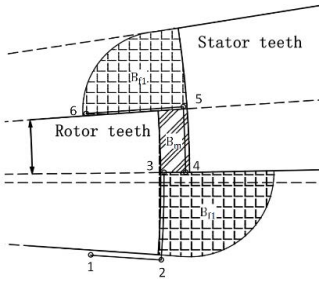

(a)

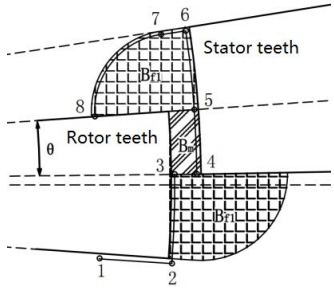

(b)

FIGURE 4. Equivalent air gap magnetic circuit at position $\theta \in [0°, 8°]$. (a) Traditional integration path. (b) Integral path of this article.

the windings. The magnetic flux generated by the windings in the magnetic circuit is indicated by Φ_{A1} and Φ_{A2} and "$\rightarrow$" indicates the direction of the flux. The number of turns per coil is 100 and is indicated by the unified symbol N. When the A-phase winding is energized, the planar equivalent magnetic circuit diagram of a pair of energized windings is shown in Fig.5.

Generally, the magnetic potential drop of any section of the magnetic circuit can be calculated by the integral of the magnetic field strength along the magnetic circuit section. Combined with Fig.4 the relationship between the magnetic potential f acting on a magnetic circuit and the magnetic field strength can be expressed as:

$$f = Ni = H_G l_0 + H_1 l_1 + H_2 l_2 \tag{5}$$

where: H_G is the magnetic field strength, l_0 is the air gap magnetic circuit length, H_1 is the magnetic field strength in the stator teeth, l_1 is the average magnetic circuit length in the stator teeth, H_2 is the magnetic field strength in the rotor teeth and l_2 is the average magnetic circuit length in the rotor teeth.

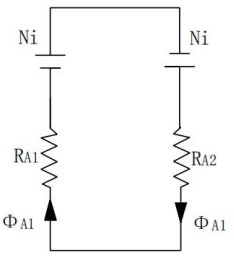

FIGURE 5. Planar equivalent magnetic circuit diagram.

The relationship between magnetic field strength H (A/m) and flux density $B(Wb/m^2)$ is usually linear. The reluctance of the core material is so small in the motor operating condition that it can be neglected. Therefore, (5) can be simplified to obtain:

$$f = Ni = \frac{B}{\mu} l_0 \tag{6}$$

The equivalent magnetic circuit formula for the phase A can be obtained from Fig.5 as:

$$\begin{cases} Ni + \Phi_{A1} R_{A1} = Ni + \Phi_{A2} \\ \Phi_{A1} = \Phi_{A2} \end{cases} \tag{7}$$

According to (7), we can obtain:

$$\Phi = \frac{Ni}{R} \tag{8}$$

As shown in Fig.4, the magnetic path of the edge flux is approximately represented as the air gap of the main flux superimposed 1 / 4 arc trajectory. The average length l_{f1} of the edge flux at $\theta \in [0°, 8°]$ is:

$$l_{f1} = \frac{\int_0^{r|\theta|} \left(l_0 + \frac{2\pi l}{4}\right) dl}{r_0 \left(\frac{2\pi}{45} - \theta\right)} = l_0 + \frac{\pi r_0 \left(\frac{2\pi}{45} - \theta\right)}{4} \tag{9}$$

The main flux B_m and edge flux B_f in the 18/15/6 Pole DSBSRM air gap flux density can be obtained by combining (6), (7), and (8) as follows:

$$B_m = \frac{\mu_0 Ni}{l_0} \tag{10}$$

$$B_f = \frac{\mu_0 Ni}{l_{f1}}, \quad \theta \in \left[0, \frac{2\pi}{45}\right] \tag{11}$$

Combining (10) and (11) with (3) and bringing in the value of τ the 18/15/6 pole DSBSRM within [0°, 8°] torque T_1 as follows:

$$T_1 = \frac{ahr_0\mu_0 N^2 i^2}{2l_0} + \frac{bhr_0^2\mu_0 N^2 i^2}{2l_{f1}^2} \times \begin{bmatrix} cos(\frac{\pi}{45}) - cos(\frac{3\pi}{45} - \theta) - (\frac{2\pi}{45} - \theta) \\ +(\frac{2\pi}{45} - \theta) sin(\frac{3\pi}{45} - \theta) - \frac{l_0}{r_0} \end{bmatrix}, \quad \theta \in \left[0, \frac{2\pi}{45}\right] \tag{12}$$

Adjustment coefficients a and b are introduced due to the structural characteristics of this motor, $a = 0.37$, $b = -2.7$ when $\theta \in [0°, 1.5°]$, $a = 0.975$, $b = 0.97$ when $\theta \in [1.5°, 8°]$. Since there are 3 pairs of torque teeth in each phase, each phase is separated by 120°. Therefore, the torque T in [0°, 8°] is:

$$T = \begin{cases} 0.111 \times K_1 - 7.767 \times K_2, & \theta \in [0°, 1.5°] \\ 0.975 \times K + 2.91 \times K_2, & \theta \in [1.5°, 8°] \end{cases}$$

$$K_1 = \frac{hr_0\mu_0 N^2 i^2}{2l_0}$$

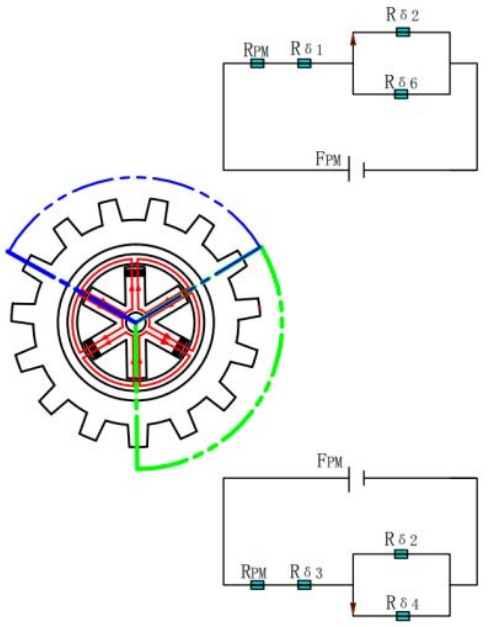

FIGURE 6. Equivalent magnetic circuit model of permanent magnets.

$$K_2 = \frac{hr_0^2\mu_0 N^2 i^2}{2l_{f1}^2} \times \left[\begin{array}{c} cos(\frac{\pi}{45}) - cos(\frac{3\pi}{45} - \theta) - (\frac{2\pi}{45} - \theta) \\ +(\frac{2\pi}{45} - \theta)sin(\frac{3\pi}{45} - \theta) - \frac{l_0}{r_0} \end{array}\right] \quad (13)$$

B. SUSPENSION SYSTEM

The inner stator and the toroidal core use the principle of differential control to generate the magnetic levitation force. Through the alternating distribution of permanent magnet and excitation, the permanent magnet provides a stable and continuous magnetic field to make the suspension stable, and the current excitation is used to supplement the magnetic force to generate the directional suspension force [11]. Fig.6 shows the magnetic force lines of the bias field provided by the permanent magnets on the inner stator of the motor, when the rotor is in the ideal position. The permanent magnetic bias field is uniformly distributed on the inner stator and the toroidal core. Fig.7 shows the magnetic field lines of force provided by the control magnetic field after energization. By superimposing or canceling the magnetic lines of force generated by the control winding and the magnetic field lines of force provided by the permanent magnets, it is possible to induce a change in magnetic flux, thus generating a magnetic levitation force. In the case of ignoring the magnetic saturation effect of the iron core, the rotor is set to deviate in the negative direction of the Y axis, and the mathematical expression of the levitation force generated in the Y axis is solved.

According to the basic theory of electromagnetic field, the magnetic levitation force F_M can be obtained by Maxwell

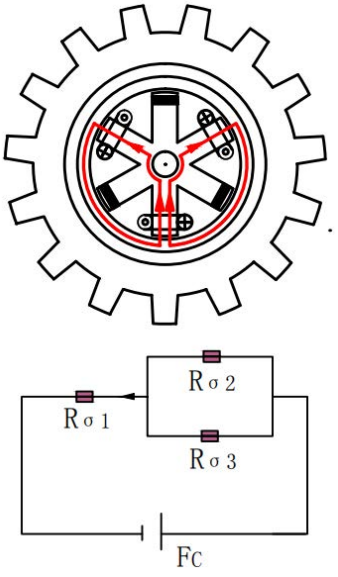

FIGURE 7. Equivalent magnetic circuit model of control winding.

stress method as follows:

$$F_M = B_M^2 A \Big/ 2\mu_0 \quad (14)$$

where: B_M is the electromagnetic induction of air gap section:

$$B_M = \Phi \Big/ A \quad (15)$$

The derivation of the mathematical model of magnetic levitation force considers the influence of rotor eccentricity. Magnetic levitation control adopts the differential control method. The permanent magnet bias magnetic field is provided by the permanent magnet. When the rotor is offset, the air gap reluctance of each magnetic circuit also changes, which causes the corresponding flux density to change. Thereby, there are:

$$\begin{cases} R_{\delta 1} = \dfrac{\delta - g_0}{\mu_0 A} \\ R_{\delta 2} = \dfrac{\delta - g_0 cos60^\circ}{\mu_0 A} \\ R_{\delta 3} = \dfrac{\delta + g_0 cos60^\circ}{\mu_0 A} \\ R_{\delta 4} = \dfrac{\delta + g_0}{\mu_0 A} \\ R_{\delta 6} = \dfrac{\delta - g_0 cos60^\circ}{\mu_0 A} \\ R_{\sigma 1} = \dfrac{\delta + g_0}{\mu_0 A} \\ R_{\sigma 2} = \dfrac{\delta + g_0 cos60^\circ}{\mu_0 A} \\ R_{\sigma 3} = R_{\sigma 2} \end{cases} \quad (16)$$

In the above equation, $R_{\delta 1}$ is the air gap reluctance of the upper permanent magnet bias flux in the +Y, $R_{\delta 2}$ is the air gap reluctance of the upper permanent magnet bias flux at an angle of 60° from +Y, $R_{\delta 3}$ is the air gap reluctance of the lower right permanent magnet bias flux at an angle of 120° from +Y, $R_{\delta 4}$ is the air gap reluctance of the lower

right permanent magnet bias flux at a position in the -Y, $R_{\delta 6}$ is the air gap reluctance of the upper permanent magnet bias flux at an angle of $-60°$ from $+Y$. $R_{\sigma 1}$ is the air gap reluctance corresponding to the control winding in the -Y, $R_{\sigma 2}$ is the air gap reluctance corresponding to the control winding at an angle of 60° from $+Y$, $R_{\sigma 3}$ is the air gap reluctance corresponding to the control winding at an angle of $-60°$ from $+Y$. δ is the thickness of the inner stator and rotor air gaps when the rotor is in the ideal position, μ_0 is the air permeability at the air gap, g_0 is the distance the rotor is offset in the negative Y direction, A is the positive area at the air gap, and R_{PM} is the permanent magnet reluctance:

$$R_{PM} = \frac{l_{PM}}{\mu_0 \mu_r l h_{PM}} \tag{17}$$

where: l_{PM} is the radial magnetization length of the permanent magnet, μ_r is the permeability of the permanent magnet, l is the width of the permanent magnet, h_{PM} is the axial length of the permanent magnet.

The magnetomotive force F_{PM} for the flux of a permanent magnet is:

$$F_{PM} = H_c l_{PM} \tag{18}$$

where: H_c is the magnetic field strength within the permanent magnet.

The magnetomotive force F_c of the magnetic flux of the control winding is:

$$F_c = Ni \tag{19}$$

where: N is the number of winding turns, i is the control winding current.

According to the equivalent magnetic circuit diagram in Fig.6 and Fig.7, the control flux Φ_{c1} in the $+Y$, the permanent magnet bias flux Φ_{PM1} in the $+Y$, and the permanent bias flux Φ_{PM2} at an angle of 120° in the $+Y$ are obtained.

$$\begin{cases} \Phi_{c1} = \dfrac{F_c/_{\sigma_1} \cdot (R_{\sigma 2} + R_{\sigma 3})}{R_{\sigma 2} R_{\sigma 3} + R_{\sigma 1} (R_{\sigma 2} + R_{\sigma 3})} \\ \Phi_{PM1} = \dfrac{F_{PM}/_{\sigma_{PM1}} \cdot R_{\delta 2}}{R_{\delta 2} R_{\delta 4} + (R_{\delta 2} + R_{\delta 4})(R_{PM} + R_{\delta 3})} \\ \Phi_{PM2} = \dfrac{F_{PM}/_{\sigma_{PM1}} \cdot R_{\delta 2}}{R_{\delta 2} R_{\delta 4} + (R_{\delta 2} + R_{\delta 4})(R_{PM} + R_{\delta 3})} \\ \qquad + \dfrac{F_{PM}/_{\sigma_{PM2}} \cdot R_{\delta 6}}{R_{\delta 2} R_{\delta 6}} \\ \qquad + (R_{\delta 2} + R_{\delta 6})(R_{PM} + R_{\delta 1}) \end{cases} \tag{20}$$

where: σ_1 is the leakage coefficient of the control flux in the -Y, σ_{PM1} is the leakage coefficient of the permanent magnet bias flux at an angle of 120° in the positive direction of the Y-axis, and σ_{PM2} is the leakage coefficient of the permanent magnet bias flux in the positive direction of the Y-axis.

Combining the above equations gives the levitation forces F_{M1} F_{M2} as:

$$F_{M1} = \frac{(2\Phi_{PM1} + \Phi_{c1})^2}{2\mu_0 A} \tag{21}$$

$$F_{M2} = \frac{\Phi_{PM2}^2}{2\mu_0 A} \tag{22}$$

The combined force F_M of the levitation forces acting on the annular core is:

$$F_M = F_{M1} - 2F_{M2} cos 60° \tag{23}$$

IV. CHARACTERISTIC ANALYSIS AND MODEL VALIDATION

In this section, in order to investigate the performance of the 18/15/6 pole DSBSRM motor, Ansoft Maxwell 2D software is used to model the motor in two dimensions [21]. In this way, the torque performance, suspension performance and decoupling performance of the motor are analyzed. The correctness of the mathematical model is verified.

A. TORQUE PERFORMANCE AND TORQUE MODEL VALIDATION

Fig.8 shows the magnetic flux density at the misalignment of the rotor teeth and stator teeth for phase A current i_A =3A. We can see that the magnetic field intensity is concentrated on the stator teeth with the energized winding and the corresponding rotor teeth. The magnetic field intensity does not affect the other stator teeth or the inner stator suspension. It indicates that good performance can be achieved without isolation between external stators or rotors.

Combined with (13), I observed that the main factors affecting the torque output when the motor size has been determined are the air gap width and the torque control current. Fig.9(a) depicts the torque characteristic curve when the torque air gap width is 0.3mm, 0.5mm, 0.7mm, and the phase A torque control current $i_A = [0A, 3A]$. The graphic analysis shows that the torque output is generally improved with the decrease of the torque air gap width. The decrease of the air gap width reduces the air gap reluctance at the same time, which conforms to the ''principle of minimum reluctance''.

Fig.9(b) depicts the torque characteristic curves derived from the Ansoft Maxwell 2D analysis and mathematical model for phase A torque control currents i_A = 1A, 2A, and 3A at a torque air gap width of 0.5 mm. Firstly, there are slight deviations between the mathematical model and the finite element simulation results at the beginning of the torque winding with different currents. This is because the rotor tooth and

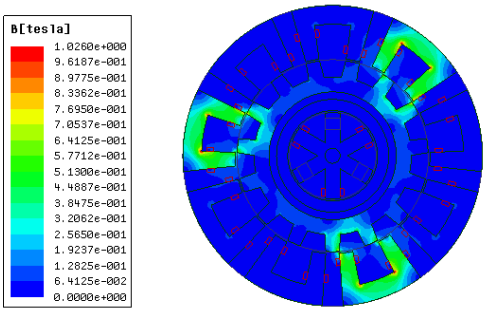

FIGURE 8. Distribution of magnetic field density at current i_A = 3A.

stator tooth are affected by many factors such as magnetic saturation and mutual inductance at the coincidence stage. The mathematical model results are basically consistent with the finite element simulation results. The correctness of the mathematical model is also verified along with the analysis of the characteristics. Secondly, the torque output is generally improved as the current increases when the air gap width is constant, and the positive torque is continued at a step angle to ensure the full cycle of the motor's forward rotation.

The normal and good operation of the bearingless switched reluctance motor needs to control the sequential start of each phase on the basis of a suitable control method. This article mainly focuses on the optimization and verification analysis of the motor structure. In order to simply reflect the comprehensive operating effect of the 18/15/6 pole DSBSRM, only in the case of a fixed opening angle, the 3 phases torque group is started in sequence and the total torque is synthesized. Fig.9(c) is a torque graph and a torque composite graph in the range of [0° ∼ 28°] when the control current of each phase is 2A. According to (24), the torque ripple value p_1 of the synthesized torque in this range is 28.84%.

$$P_1 = \frac{T_{max} - T_{min}}{T_{ave}} \tag{24}$$

where: T_{max}, T_{min} and T_{ave} are the maximum, minimum and average values of torque in the sampling interval.

B. SUSPENSION PERFORMANCE AND TORQUE MODEL VALIDATION

Fig.10 shows the magnetic field density distribution generated by the permanent magnet and the magnetic field density distribution generated when the control winding M_3 passes through 3A current. The graphic analysis shows that the magnetic field intensity generated by the suspension system is mainly concentrated on the inner stator and rotor ring core and does not affect the external stator and torque rotor.

From the 2.2 levitation force mathematical model analysis, I observed that the thickness of the levitation air gap, the levitation control current, the radial magnetization length and the rotor offset are the main factors affecting the magnitude of the levitation force. In order to carry out its characteristic analysis and verify the correctness of the mathematical model, the simulation results of the levitation output value in the Y direction generated under the control winding M_3 current of 0∼3A and the calculation results of the mathematical model are plotted in Fig.11 (The positive Y direction is taken as positive).

Fig.11 (a) describes the levitation force values under different air gap thicknesses. We can see that the average levitation force values under the air gap width of 0.4mm, 0.5mm, and 0.6mm when the current is 3A are 215N, 157N, 121N respectively. Calculated by (25), the levitation force pulsation in the sampling interval when the control current is 3A is 0.081%, 0.052%, and 0.41% respectively. The magnitude of the levitation force increases as the air gap thickness decreases. The levitation force value remains constant when the rotor angle

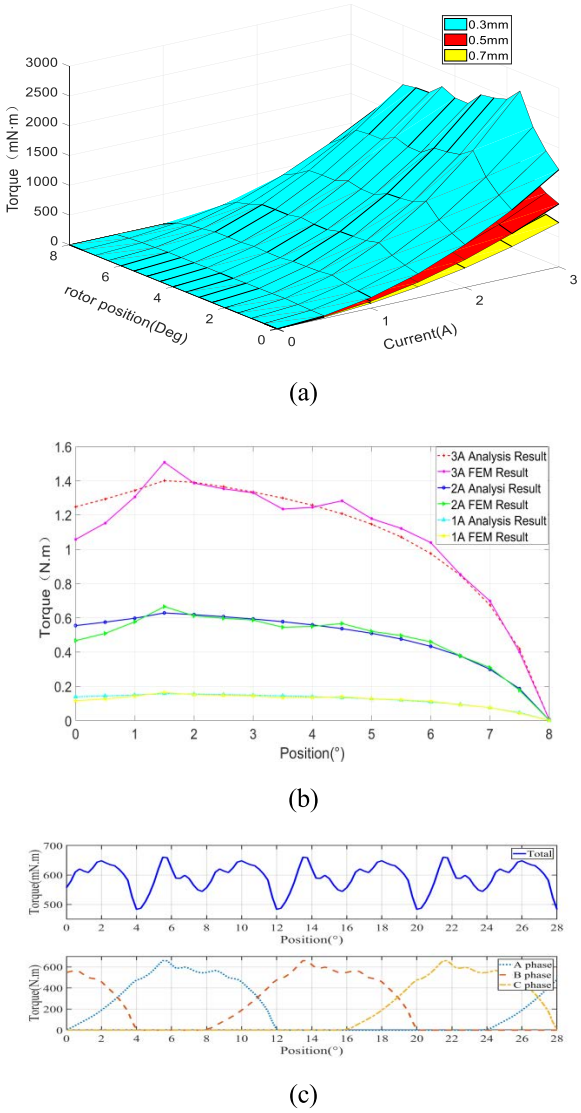

FIGURE 9. Torque characteristics. (a)Surface diagram of torque characteristics. (b) Torque characteristic curve. (c) Torque synthesis graph.

changes, ensuring the stability of the suspension control.

$$P_2 = \frac{F_{max} - F_{min}}{F_{ave}} \times 100\% \tag{25}$$

where: F_{max}, F_{min} and F_{ave} are the maximum, minimum, and average values floating in the sampling interval.

Fig.11(b) shows the simulated and mathematical model calculated values of the levitation force when the rotor is offset in the Y axis (taking the negative direction of movement as positive). The values of suspension force at the offset of −0.1mm, 0mm, 0.1mm and 0.2mm are 35N, 0N, −32N, and −64N respectively in the case of control current of 0A. Combining the formulas in Fig.11 and the formula in section 2.2, we can see that when the rotor moves to the negative direction, the air gap thickness in the positive direction of the Y axis decreases, and the air gap reluctance decreases. The levitation

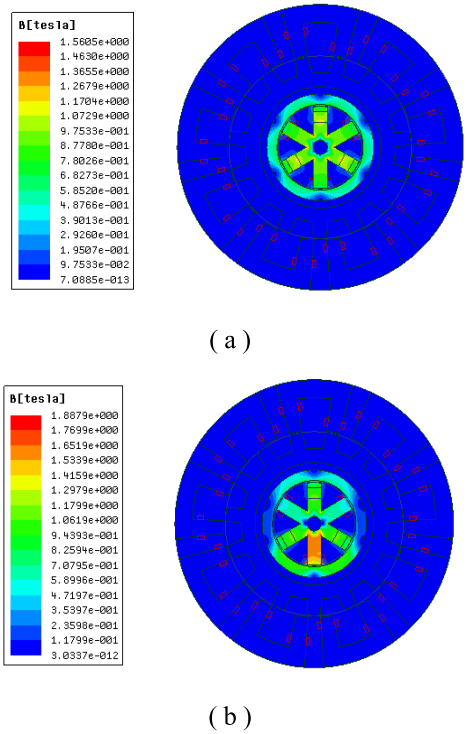

FIGURE 10. Magnetic field density distribution of suspension system. (a) Density distribution of permanent magnetic bs. (b) Distribution of magnetic field density of control winding.

force in the negative direction is generally generated, and vice versa. From the equation in section 2.2, I observed that the levitation force is proportional to the square of the current. However, due to the relatively small magnetic field intensity produced by the low current, the suspended output value in Fig.11(b) shows an approximate linear relationship with the current. In turn, the correctness of the mathematical model is verified.

Fig.11 (c) shows the levitation force output at different radial magnetization lengths. This is due to the fact that the radial magnetization length of 1.5 mm is basically saturated in this structure. However, we can still analyze that the overall force output increases as the radial magnetization length increases.

C. DECOUPLING PERFORMANCE ANALYSIS

As Fig.12 shows the magnetic field density when the torque winding and suspension winding are energized simultaneously. We can see that the flux paths of the torque control system and suspension control system are independent of each other.

Because the torque winding of the 18/15/6 pole DSBSRM motor is centered symmetrical with the 3 pairs of poles in each phase spaced 120° apart. Therefore, the levitation force generated during torque drive will cancel each other out. Fig.13 shows the levitation force generated by the torque system at $I_A = 0{\sim}3$A and its proportion in the levitation force generated by the suspension system at $I_{M3} = 0{\sim}3$A

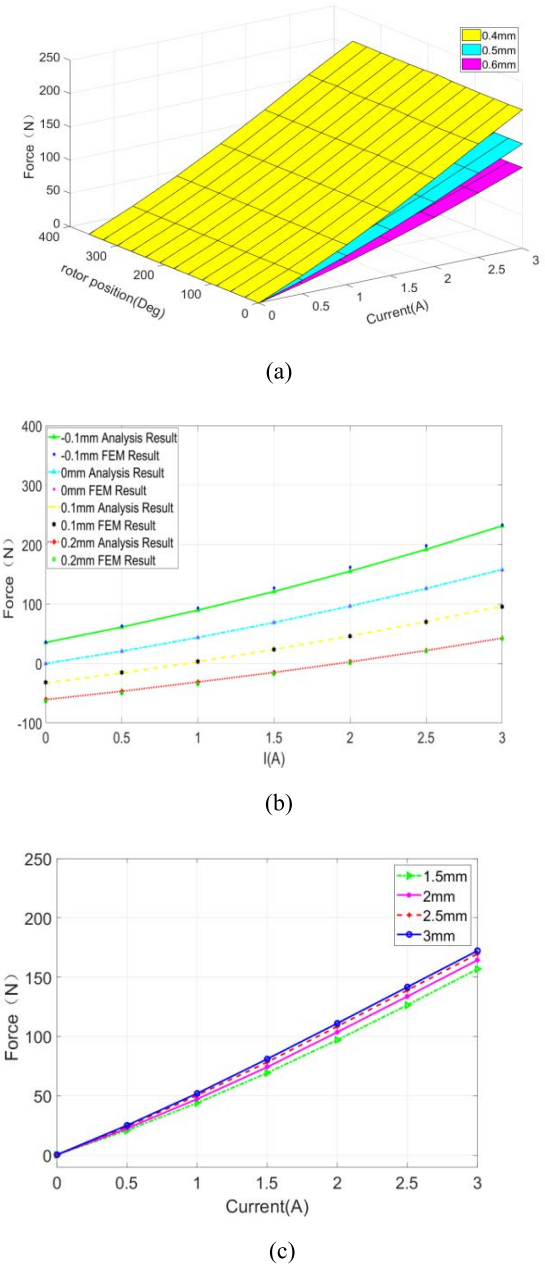

FIGURE 11. Suspension characteristics. (a) Suspension characteristics at different air gap thicknesses. (b) Suspension characteristics at different rotor offsets. (c) Suspension characteristics at different radial magnetization lengths.

in the Y-axis direction in a step angle. As can be seen from Fig.13, the maximum levitation force generated at a torque winding current of 3A does not exceed 0.5N. The maximum suspension force generated in the torque winding is 1.45 % of the suspension force generated in the suspension winding. The average levitation force generated by the torque winding accounts for the maximum of 0.106% of the levitation winding. It meets the requirement that the decoupling ratio of BSRM is less than 5%. This proves that the motor has good performance in terms of decoupling the levitation force from the torque.

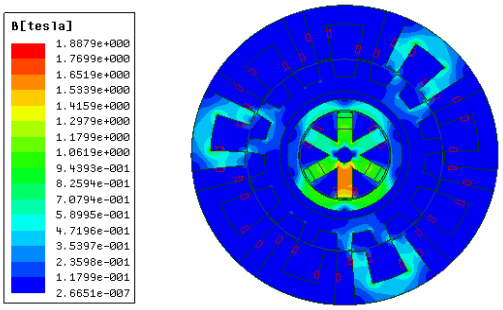

FIGURE 12. Magnetic field density when energized simultaneously.

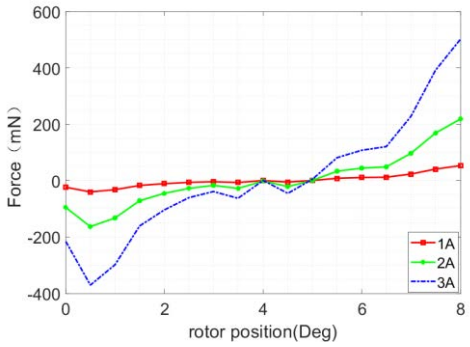

(a)

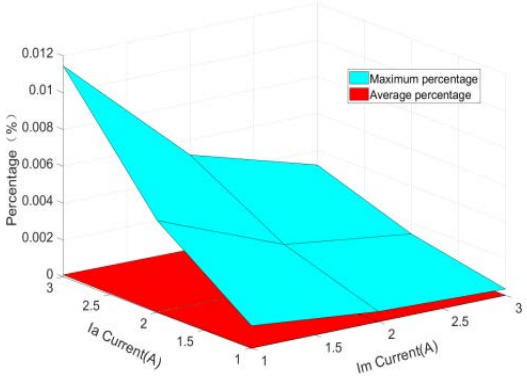

(b)

FIGURE 13. Torque and suspension decoupling performance.
(a) Levitation forces generated in the torque winding at different currents.
(b) Percentage of levitation force generated by the torque windin.

The coupling of levitation force is also an important aspect that needs to be considered, which is related to the stability of the levitation system. From Fig.14(a), we can see that the maximum levitation force in the X-direction generated by the control winding with a current of 0∼3A does not exceed 200mN. Fig.14(b) shows the levitation force generated in the Y-direction and X-direction when the control winding current is 3A. We can see that the percentage of the levitation force in the X-direction is particularly small, and the maximum percentage is 0.21%, which proved that there is almost no coupling between the X direction and the Y direction of the levitation force. The suspension system has good stability.

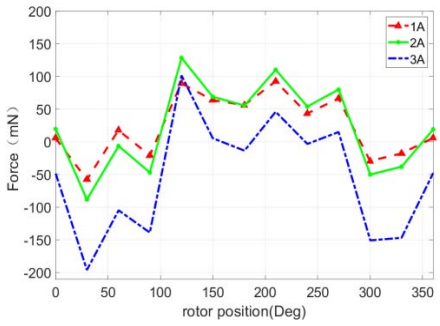

(a)

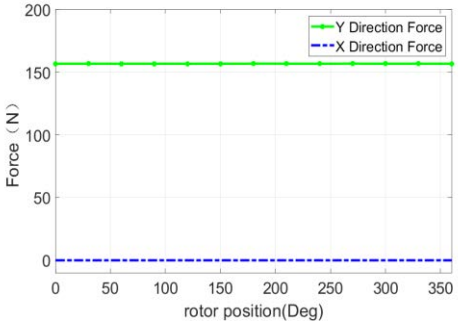

(b)

FIGURE 14. Levitation forces coupled in the x, y direction.
(a) X-directional levitation force generated by M_3 with 0-3A current.
(b) X-directional levitation force and Y-directional levitation force generated at M_3 through 3A current.

In summary, the 18/15/6 pole DSBSRM can ensure that the torque control system and the suspension control system work independently of each other. The stability of the motor is well guaranteed.

V. PERFORMANCE COMPARISONS

In order to further reflect the good performance of 18/15/6 pole DSBSRM, the new 12/8/4 pole DSBSRM with the same double stator structure [11] and the new 16 phase BSRM with decoupled structure [13] were selected for comparison. Main parameters of each motor such as air gap, height of stator and rotor, outer diameter of stator and rotor, number of windings turns and axial length of motor are basically consistent. The operating cycle, energization mode, stator-rotor pole arc and other parameters of the 3 motors are shown in Table 1, and the motor structure is shown in Fig.15.

The new 16-phase BSRM performs a phase change in the [0°, 7.5°] interval. Rotor teeth adopt block mixed tooth structure. The torque teeth and the suspension teeth are separated from each other and are sequentially embedded on the support structure. The torque teeth are set in a ‘‘U’’ shape with grooves in the teeth to increase the torque output capacity. The new 16-phase BSRM controls the torque and the radial suspension separately. It has been shown to be well decoupled. However, the torque can only be provided by one of the ’U’ teeth. There is a small torque and

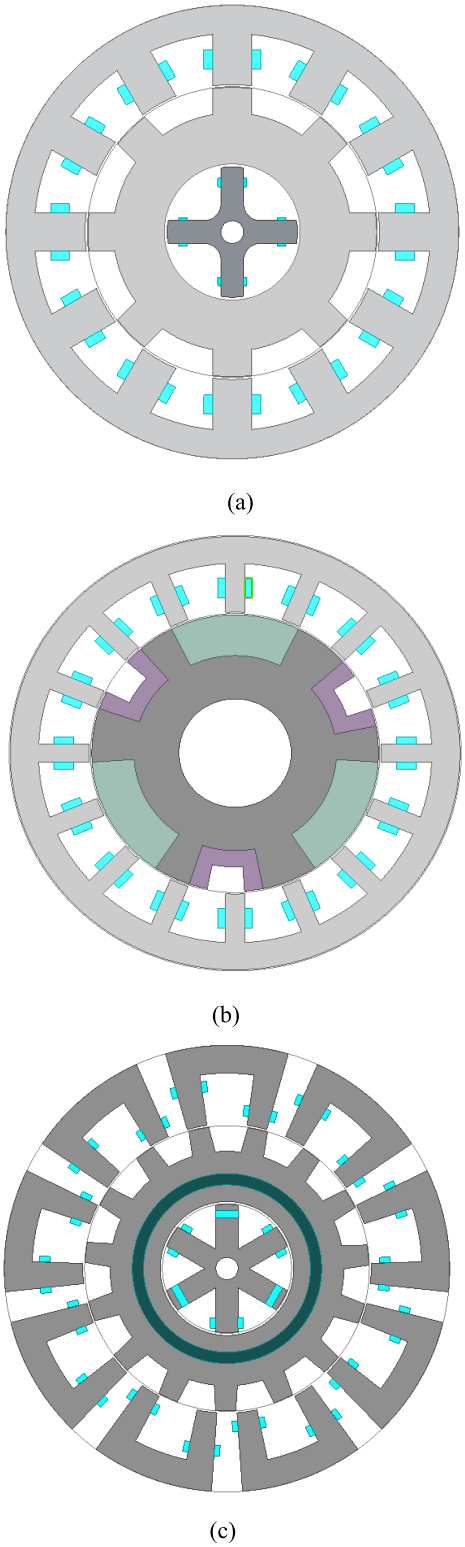

FIGURE 15. Schematic diagram of structurally decoupled BSRMs. (a) 12/8/4 pole DSBSRM. (b) New 16-phase BSRM. (c) 18/15/6 pole DSBSRM.

structural asymmetry. The 12/8/4 pole DSBSRM is based on the traditional 12/8 pole BSRM with a double stator structure. It is capable of good torque and suspension decoupling.

TABLE 1. Parameters of the 3 BSRMs.

Parameters	N12/8DS BSRM	N16B SRM	18/15/6D SBSRM
Outer diameter of outer stator	80mm	80mm	80mm
Internal diameter of external stator	52mm	52mm	52mm
rotor cooling diameter	51mm	51mm	51mm
Inner diameter of rotor	24mm	24mm	24mm
Torque tooth height	9mm	9mm	9mm
suspended tooth height	/	9mm	/
outer diameter of inner stator	23mm	/	23mm
Inner diameter of inner stator	4mm	/	4mm
Thickness of external stator yoke	5mm	5mm	5mm
Thickness of inner stator yoke	4mm	/	4mm
Ring core thickness	/	/	6mm
Airgap thickness	0.5mm	0.5mm	0.5mm
Axial length of motor	100mm	100mm	100mm
Torque tooth pole arc	15°	7.5°	8°
External stator tooth pole arc	15°	7.5°	8°
Internal stator tooth pole arc	20°	/	20°
Length of magnetization direction of permanent magnet	/	/	1.5mm
Torque winding turns	100	100	100

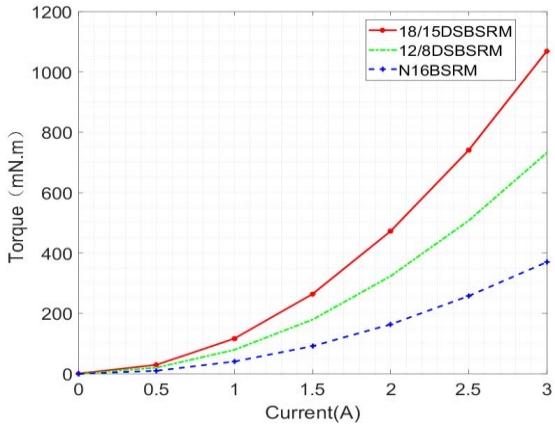

FIGURE 16. Torque comparison chart.

However, in practical engineering, the stator yoke thickness does not meet the decoupling requirements. For torque winding currents i = [0A, 3A], the average torque curves of the three motors within one stepping angle are shown in Fig.16. For suspension winding currents i = [0A, 3A], the average levitation force curve generated by the 3 motors over one cycle is shown in Fig.17.

According to Fig.16, the average torque provided by 18/15/6 pole DSBSRM at different currents within a stepping angle is significantly higher than the other two motors. The average torque provided by this motor is calculated to be 150% and 288% of the average torque of the 12/8/4

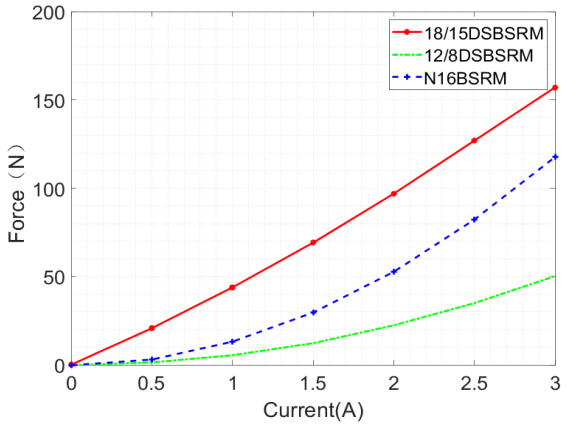

FIGURE 17. Comparison of average levitation forces.

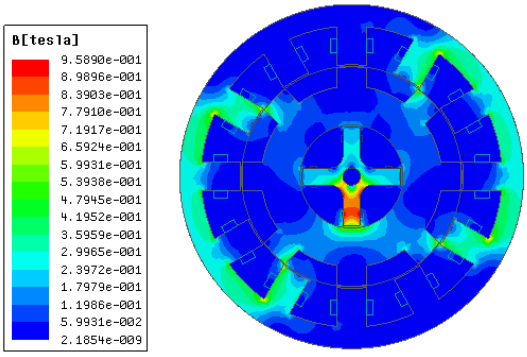

FIGURE 18. 12/8-Pole DSBSRM magnetic field density.

pole DSBSRM and the new 16-phase BSRM respectively. The 18/15/6 pole DSBSRM can provide relatively larger torque with better driving force. However, the 18/15/6 pole DSBSRM gives up the stability of the torque output while improving the torque regulation. This is determined by the nature and structure of the motor.

The comparison of the average radial levitation force of the 3 motors shown in Fig.17. We can see that the radial levitation force output of the 18/15/6 pole DSBSRM is significantly greater than that of the other two motor.

As Fig.18 shows the magnetic field density of 12/8/4 pole DSBSRM in the case of both torque control current and suspension control current of 3A. We can see that the magnetic flux lines generated by the torque system and suspension system interfere with each other. Compared to Fig.12, it proves that the 18/15/6 pole DSBSRM proposed in this paper has more excellent decoupling performance compared with 12/8/4 pole DSBSRM, which makes the control more convenient.

VI. CONCLUSION

Based on the decoupling of the BSRM, this paper proposes a new BSRM structure with the aim of improving the performance of the BSRM. By optimizing the distribution and number of stator and rotor tooth poles, the hysteresis force existing during the commutation of the electromagnetic poles is effectively reduced, and the electromagnetic conversion efficiency is significantly improved. And on the basis of the new structure, the hybrid excitation mode is adopted. Through the integrated work of permanent magnet and excitation, it not only improves the anti-interference performance of the rotor under ideal working conditions, but also enhances the suspension force output capacity. The structure is optimized for the coupling problem of torque and radial levitation force control that exists in conventional BSRM. The torque system and suspension system basically have no magnetic field coupling during operation, and the influence of torque on suspension is only 0.21%. A more accurate mathematical model based on Maxwell's stress method was established. Combined with the mathematical model to verify and analyze the impact of important parameters such as current and air gap width on the performance of the motor. By comparing with the same structure decoupling BSRM, it is proved that under the same size, the average torque output performance of this motor is improved by at least 150%. The average suspension output performance is improved by more than 200% overall. It is proved that the proposed motor structure can decouple torque and levitation force in structure. And has better torque and levitation output ability. It ensures that the motor has more prominent torque output under the condition of more stable operation and reduces the difficulty of motor control to save costs for further application. We hope to lay the foundation for the application in the field of artificial hearts in the future.

REFERENCES

[1] T. Halmeaho, T. Haarnoja, A. Manninen, J. Pippuri, J. Keranen, and K. Tammi, "Magnetic bearing as switched reluctance motor–feasibility study for bearingless switched reluctance motor," in *Proc. Int. Electric Mach. Drives Conf.*, Chicago, IL, USA, May 2013, pp. 401–408, doi: 10.1109/IEMDC.2013.6556128.

[2] A. Laiho, K. Tammi, A. Burakov, A. Arkkio, and K. Zenger, "A built-in force actuator for active control of lateral rotor vibration in cage induction electrical machines," *J. Sound Vibrat.*, vol. 320, no. 3, pp. 496–515, Feb. 2009, doi: 10.1016/j.jsv.2008.08.003.

[3] W. Zhang and H. Zhu, "Radial magnetic bearings: An overview," *Results Phys.*, vol. 7, pp. 3756–3766, Jan. 2017, doi: 10.1016/j.rinp.2017.08.043.

[4] X. Sun, L. Chen, and Z. Yang, "Overview of bearingless induction motors," *Math. Problems Eng.*, vol. 2014, pp. 1–10, Aug. 2014, doi: 10.1155/2014/570161.

[5] C. Sun, H. Yang, S. Han, H. Ding, J. Li, and N. Han, "Control system design for 16/6/8 double-stator bearingless switched reluctance motor," *Math. Problems Eng.*, vol. 2021, pp. 1–15, Aug. 2021, doi: 10.1155/2021/4727917.

[6] T. Fukao, "The evolution of motor drive technologies. Development of bearingless motors," in *Proc. IPEMC. 3rd Int. Power Electron. Motion Control Conf.*, Aug. 2000, pp. 33–38, doi: 10.1109/IPEMC.2000.885328.

[7] C. R. Morrison, M. W. Siebert, and E. J. Ho, "Electromagnetic forces in a hybrid magnetic-bearing switched-reluctance motor," *IEEE Trans. Magn.*, vol. 44, no. 12, pp. 4626–4638, Dec. 2008, doi: 10.1109/TMAG.2008.2002891.

[8] X. Diao, H. Zhu, Y. Qin, and Y. Hua, "Torque ripple minimization for bearingless synchronous reluctance motor," *IEEE Trans. Appl. Supercond.*, vol. 28, no. 3, pp. 1–5, Apr. 2018, doi: 10.1109/TASC.2018.2798632.

[9] X. Ye and W. Zixin, "Levitation performances analysis of a novel bearingless switched reluctance motor," *IEEE Trans. Appl. Supercond.*, vol. 31, no. 8, pp. 1–4, Nov. 2021, doi: 10.1109/TASC.2021.3091122.

[10] P. N. Rao, G. V. S. K. Rao, and G. V. N. Kumar, "A novel technique for controlling speed and position of bearingless switched reluctance motor employing sensorless sliding mode observer," *Arabian J. Sci. Eng.*, vol. 43, no. 8, pp. 4327–4346, Aug. 2018, doi: 10.1007/s13369-017-3027-8.
[11] C. Sun, J. Li, H. Ding, H. Yang, S. Han, and N. Han, "Characteristic analysis of a new double stator bearingless switched reluctance motor," *IEEE Access*, vol. 9, pp. 38626–38635, 2021, doi: 10.1109/ACCESS.2021.3064017.
[12] C. Sun, J. Li, P. Zhuang, and J. Li, "Design and analysis of a novel 24-phase bearingless switched reluctance motor," in *Proc. IEEE 3rd Int. Electr. Energy Conf. (CIEEC)*, Sep. 2019, pp. 451–455, doi: 10.1109/CIEEC47146.2019.CIEEC-2019200.
[13] C. Sun, P. Zhuang, J. Li, and J. Li, "Design and analysis of a 16/6 bearingless switched reluctance motor with segment hybrid rotor teeth," *IEEJ Trans. Elect. Electron. Eng.*, vol. 15, no. 6, pp. 939–946, Jun. 2020.
[14] Z. Xu, F. Zhang, and J.-W. Ahn, "Design and analysis of a novel 12/14 hybrid pole type bearingless switched reluctance motor," in *Proc. IEEE Int. Symp. Ind. Electron.*, May 2012, pp. 1922–1927, doi: 10.1109/ISIE.2012.6237386.
[15] W. Peng, Z. Xu, D.-H. Lee, and J.-W. Ahn, "Control of radial force in double stator type bearingless switched reluctance motor," *J. Electr. Eng. Technol.*, vol. 8, no. 4, pp. 766–772, Jul. 2013, doi: 10.5370/JEET.2013.8.4.766.
[16] C. Hao, "Research on the control method of single winding compound rotor bearingless switched reluctance motor," M.S. thesis, Nanjing Univ. Posts Telecommun., Nanjing, China, 2019. Accessed: Oct.5, 2021. [Online]. Available: https://kns.cnki.net/kcms/detail/detail.aspx?dbcode=CMFD&dbname=CMFD202001&filename=1019692038.nh&uniplatform=NZKPT&v=Lq4Jip%25mmd2B3YetPymM32vhvVTEY%25mmd2F7ipOPCU9Dmro3fQWUuXADlcg80LXl5HV3HvgLUn
[17] J. Zhang, H. Wang, S. Zhu, and T. Lu, "Multi-physics multi-objective optimal design of bearingless switched reluctance motor based on finite-element method," *Energies*, vol. 12, no. 12, p. 2374, Jun. 2019, doi: 10.3390/en12122374.
[18] W. Ding, S. Yang, and Y. Hu, "Development and investigation on segmented-stator hybrid-excitation switched reluctance machines with different rotor pole numbers," *IEEE Trans. Ind. Electron.*, vol. 65, no. 5, pp. 3784–3794, May 2018, doi: 10.1109/TIE.2017.2760846.
[19] X. Wang, B. Ge, J. Wang, and F. J. T. E. Ferreira, "Radial force analytic modeling for a novel bearingless switched reluctance motor when considering rotor eccentricity," *Electr. Power Compon. Syst.*, vol. 42, no. 6, pp. 544–553, Apr. 2014, doi: 10.1080/15325008.2014.880968.
[20] M. Takemoto, A. Chiba, H. Akagi, and T. Fukao, "Radial force and torque of a bearingless switched reluctance motor operating in a region of magnetic saturation," *IEEE Trans. Ind. Appl.*, vol. 40, no. 1, pp. 103–112, Jan. 2004, doi: 10.1109/TIA.2003.821816.
[21] Q. Yin, H. Runke, Z. Long, and W. Lei, "Simulation of switched reluctance motor characteristics based on Maxwell2D," *Motors Control Appl.*, vol. 39, no. 10, pp. 5–8, 2012.

NING HAN received the B.S. degree in mechanical design manufacture and automation from Qingdao Huanghai University, China. He is currently pursuing the M.S. degree in mechanical engineering with the Shandong University of Science and Technology, China.

CHUANYU SUN received the M.S. and Ph.D. degrees from the Shandong University of Science and Technology, China, in 2007 and 2010, respectively. His research interests include magnetic suspending artificial heart and magnetic suspending control systems.

JIAQING LI received the B.S. degree in mechanical design manufacture and automation from Zaozhuang University, China. He is currently pursuing the M.S. degree in mechanical engineering with the Shandong University of Science and Technology, China.

HANG YANG received the B.S. degree in measurement and control technology and instrument from the Shandong University of Science and Technology, China, where he is currently pursuing the M.S. degree in testing and measuring technology and instruments.

SHANGKE HAN received the B.S. degree in measurement and control technology and instrument from the Shandong University of Science and Technology, China, where she is currently pursuing the M.S. degree in testing and measuring technology and instruments.